



# Performance of the LHCb Outer Tracker

The LHCb Outer Tracker group

R. Arink<sup>1</sup>, S. Bachmann<sup>2</sup>, Y. Bagaturia<sup>2</sup>, H. Band<sup>1</sup>, Th. Bauer<sup>1</sup>, A. Berkien<sup>1</sup>, Ch. Färber<sup>2</sup>, A. Bien<sup>2</sup>, J. Blouw<sup>2</sup>, L. Ceelie<sup>1</sup>, V. Coco<sup>1</sup>, M. Deckenhoff<sup>3</sup>, Z. Deng<sup>7</sup>, F. Dettori<sup>1</sup>, D. van Eijk<sup>1</sup>, R. Ekelhof<sup>3</sup>, E. Gersabeck<sup>2</sup>, L. Grillo<sup>2</sup>, W.D. Hulsbergen<sup>1</sup>, T.M. Karbach<sup>3,4</sup>, R. Koopman<sup>1</sup>, A. Kozlinskiy<sup>1</sup>, Ch. Langenbruch<sup>2</sup>, V. Lavrentyev<sup>1</sup>, Ch. Linn<sup>2</sup>, M. Merk<sup>1</sup>, J. Merkel<sup>3</sup>, M. Meissner<sup>2</sup>, J. Michalowski<sup>5</sup>, P. Morawski<sup>5</sup>, A. Nawrot<sup>6</sup>, M. Nedos<sup>3</sup>, A. Pellegrino<sup>1</sup>, G. Polok<sup>5</sup>, O. van Petten<sup>1</sup>, J. Rövekamp<sup>1</sup>, F. Schimmel<sup>1</sup>, H. Schuylenburg<sup>1</sup>, R. Schwemmer<sup>2,4</sup>, P. Seyfert<sup>2</sup>, N. Serra<sup>1</sup>, T. Sluijk<sup>1</sup>, B. Spaan<sup>3</sup>, J. Spelt<sup>1</sup>, B. Storaci<sup>1</sup>, M. Szczekowski<sup>6</sup>, S. Swientek<sup>3</sup>, S. Tolk<sup>1</sup>, N. Tuning<sup>1</sup>, U. Uwer<sup>2</sup>, D. Wiedner<sup>2</sup>, M. Witek<sup>5</sup>, M. Zeng<sup>7</sup>, A. Zwart<sup>1</sup>.

<sup>1</sup>*Nikhef, Amsterdam, The Netherlands*

<sup>2</sup>*Physikalisches Institut, Heidelberg, Germany*

<sup>3</sup>*Technische Universität Dortmund, Germany*

<sup>4</sup>*CERN, Geneva, Switzerland*

<sup>5</sup>*H. Niewodniczanski Institute of Nuclear Physics, Cracow, Poland*

<sup>6</sup>*A. Soltan Institute for Nuclear Studies, Warsaw, Poland*

<sup>7</sup>*Tsinghua University, Beijing, China*

## Abstract

The LHCb Outer Tracker is a gaseous detector covering an area of  $5 \times 6 \text{ m}^2$  with 12 double layers of straw tubes. The detector with its services are described together with the commissioning and calibration procedures. Based on data of the first LHC running period from 2010 to 2012, the performance of the readout electronics and the single hit resolution and efficiency are presented.

The efficiency to detect a hit in the central half of the straw is estimated to be 99.2%, and the position resolution is determined to be approximately 200  $\mu\text{m}$ . The Outer Tracker received a dose in the hottest region corresponding to 0.12 C/cm, and no signs of gain deterioration or other ageing effects are observed.

Published in JINST

© CERN on behalf of the LHCb collaboration, license CC-BY-3.0.



# Contents

<b>1</b>	<b>Introduction</b>	<b>2</b>
<b>2</b>	<b>Services performance</b>	<b>5</b>
2.1	Gas system . . . . .	5
2.2	Gas monitoring . . . . .	6
2.3	Low voltage . . . . .	7
2.4	High voltage . . . . .	7
<b>3</b>	<b>Commissioning and monitoring</b>	<b>8</b>
3.1	Quality assurance of detector modules and C-frame services . . . . .	8
3.2	Noise . . . . .	9
3.3	Threshold scans . . . . .	10
3.4	Delay scans . . . . .	10
<b>4</b>	<b>Calibration</b>	<b>11</b>
4.1	Distance drift-time relation . . . . .	11
4.2	$t_0$ stability . . . . .	14
4.3	Geometrical survey . . . . .	14
4.4	Optical alignment with the Rasnik system . . . . .	15
4.5	Software alignment . . . . .	16
<b>5</b>	<b>Performance</b>	<b>18</b>
5.1	Spillover and drift-time spectrum . . . . .	18
5.2	Occupancy . . . . .	20
5.3	Hit efficiency . . . . .	21
5.4	Hit resolution . . . . .	24
5.5	Monitoring of faulty channels . . . . .	25
5.6	Radiation tolerance . . . . .	26
<b>6</b>	<b>Conclusions</b>	<b>27</b>
	<b>References</b>	<b>28</b>

# 1 Introduction

The LHCb detector [1] is a single-arm forward spectrometer covering the pseudo-rapidity range  $2 < \eta < 5$ , designed for the study of particles containing  $b$  or  $c$  quarks. The detector includes a high-precision tracking system consisting of a silicon-strip vertex detector surrounding the  $pp$  interaction region, a large-area silicon-strip detector located upstream of a dipole magnet with a bending power of about 4 Tm and three tracking stations located downstream. The area close to the beamline is covered by silicon-strip detectors, whereas the large area at more central rapidity is covered by the Outer Tracker (OT) straw-tube detector.

Excellent momentum resolution is required for a precise determination of the invariant mass of the reconstructed  $b$ -hadrons. For example a mass resolution of 25 MeV/ $c^2$  for the decay  $B_s^0 \rightarrow \mu^+\mu^-$  translates into a required momentum resolution of  $\delta p/p \approx 0.4\%$  [2]. Furthermore, the reconstruction of high-multiplicity  $B$  decays demands a high tracking efficiency and at the same time a low fraction of wrongly reconstructed tracks. To achieve the physics goals of the LHCb experiment, the OT is required to determine the position of single hits with a resolution of 200  $\mu\text{m}$  in the  $x$ -coordinate<sup>1</sup>, while limiting the radiation length to 3%  $X_0$  per station (see Fig. 1b). A fast counting gas is needed to keep the occupancy below 10% at the nominal luminosity of  $2 \times 10^{32} \text{ cm}^{-2}\text{s}^{-1}$ .

The OT is a gaseous straw tube detector [3] and covers an area of approximately  $5 \times 6 \text{ m}^2$  with 12 double layers of straw tubes. The straw tubes are 2.4 m long with 4.9 mm inner diameter, and are filled with a gas mixture of Ar/CO<sub>2</sub>/O<sub>2</sub> (70/28.5/1.5) which guarantees a fast drift-time below 50 ns. The anode wire is set to +1550 V and is made of gold plated tungsten of 25  $\mu\text{m}$  diameter, whereas the cathode consists of a 40  $\mu\text{m}$  thick inner foil of electrically conducting carbon doped Kapton-XC<sup>2</sup> and a 25  $\mu\text{m}$  thick outer foil, consisting of Kapton-XC laminated together with a 12.5  $\mu\text{m}$  thick layer of aluminium. The straws are glued to sandwich panels, using Araldite AY103-1<sup>3</sup>. Two panels are sealed with 400  $\mu\text{m}$  thick carbon fiber sidewalls, resulting in a gas-tight box enclosing a stand-alone detector module. A cross-section of the module layout is shown in Fig. 1(a).

The modules are composed of two staggered layers (monolayers) of 64 drift tubes each. In the longest modules (type  $F$ ) the monolayers are split in the middle into two independent readout sections composed of individual straw tubes. Both sections are read out from the outer ends. The splitting in two sections is done at a different position for the two monolayers to avoid insensitive regions in the middle of the module.  $F$ -modules have an active length of 4850 mm and contain twice 128 straws, in the upper and the lower half, respectively. Short modules (type  $S$ ) have about half the length of  $F$ -type modules and are mounted above and below the beampipe. They contain 128 single drift

---

<sup>1</sup> The LHCb coordinate system is a right-handed coordinate system, with the  $z$  axis pointing along the beam axis,  $y$  is the vertical direction, and  $x$  is the horizontal direction. The  $xz$  plane is the bending plane of the dipole magnet.

<sup>2</sup> Kapton® is a polyimide film developed by DuPont.

<sup>3</sup> Araldite® is a two component epoxy resin developed by Huntsman.

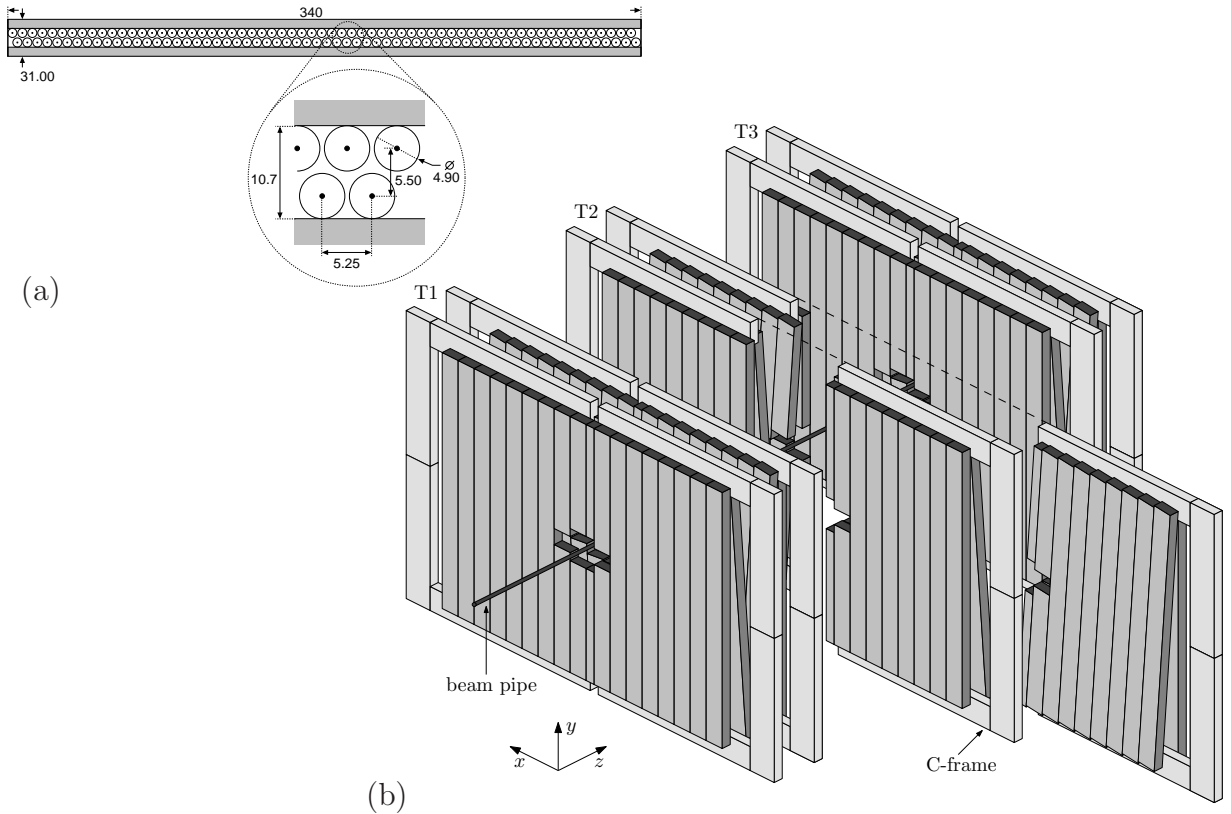


Figure 1: (a) Module cross section. (b) Arrangement of OT straw-tube modules in layers and stations.

tubes, and are read out only from the outer module end. The inner region not covered by the OT,  $|y| < 10(20)$  cm for  $|x| < 59.7(25.6)$  cm, is instrumented with silicon strip detectors [1]. One detector layer is built from 14 long and 8 short modules, see Fig. 1(b). The complete OT detector consists of 168 long and 96 short modules and comprises 53,760 single straw-tube channels.

The detector modules are arranged in three stations. Each station consists of four module layers, arranged in an  $x$ - $u$ - $v$ - $x$  geometry: the modules in the  $x$ -layers are oriented vertically, whereas those in the  $u$  and  $v$  layers are tilted by  $+5^\circ$  and  $-5^\circ$  with respect to the vertical, respectively. This leads to a total of 24 straw layers positioned along the  $z$ -axis.

Each station is split into two halves, retractable on both sides of the beam line. Each half consists of two independently movable units, known as C-frames, see Fig. 1(b). The modules are positioned on the C-frames by means of precision dowel pins. The C-frames also provide routing for all detector services (gas, low and high voltage, water cooling, data fibres, slow and fast control). The OT C-frames are sustained by a stainless steel structure (OT bridge), equipped with rails allowing the independent movement of all twelve C-frames. At the top the C-frames hang on the rails, while at the bottom the

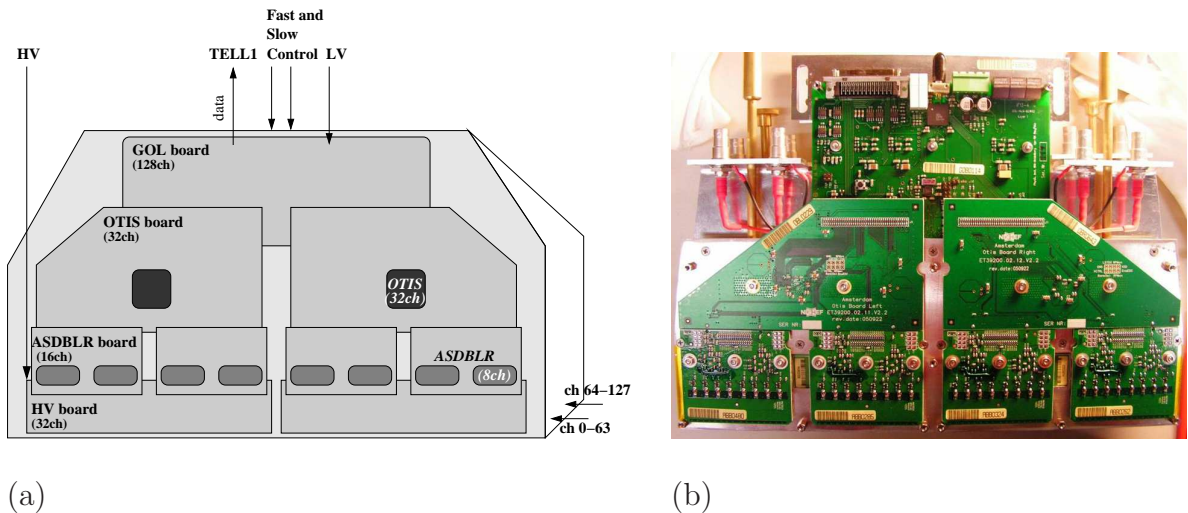


Figure 2: (a) Design and (b) photograph of the FE electronics mounted in a FE box. Only the boards that read out one monolayer of 64 straws are visible. In addition, the HV boards are not visible in the photograph as they are hidden by the ASDBLR boards.

C-frames are guided, but not supported by the rails, to constrain the movement in the  $z$ -coordinate.

The front-end (FE) electronics measures the drift-times of the ionization clusters produced by charged particles traversing the straw-tubes with respect to the beam crossing (BX) signal [4]. The drift-times are digitized for each 25 ns (the LHC design value for the minimum bunch crossing interval) and stored in a digital pipeline to await the lowest-level trigger (L0) decision. On a positive L0 decision, the digitized data in a window of 75 ns is transmitted via optical links to TELL1 boards in the LHCb DAQ system [5].

As shown in Fig. 2, the FE electronics has a modular design, consisting of several interconnected boards housed inside a metallic box (FE box). The main components of the OT readout electronics are the high voltage (HV) board, the ASDBLR amplifier board, the OTIS digitization board, and the GOL auxiliary (GOL/AUX) board. Each ASDBLR board hosts two ASDBLR chips [6]. These are custom-made integrated circuits, providing the complete analog signal processing chain (amplification, shaping, baseline restoration, and discrimination) for the straw tube detectors. The hit outputs of two ASDBLR boards (32 channels) are connected to one OTIS board, which hosts one radiation-hard OTIS TDC chip for drift-time digitization [7,8]. The time digitization is done through the 25 ns long Delay Locked Loop (DLL) using the 64 delay-stages of the DLL (64 time bins), giving a step size of about 0.4 ns.

The drift-time data is stored in a pipeline memory with a depth of 164 events, corresponding to a latency of 4.1  $\mu$ s. If a trigger occurs, the corresponding data words of up to 3 bunch crossings are transferred to a derandomizing buffer, able to store data from up to 16 consecutive triggers. Only the first hit in the 75 ns wide window of a given channel is stored. Later signals from multiple ionizations or reflections are thus not recorded. The

OTIS boards in a FE box are connected to one GOL/AUX board. This board [9] provides the outside connections to the FE box: the power connection, the interface to the fast-control (beam crossing clock BX, triggers, resets) and the interface to the slow-control (I<sup>2</sup>C).

These boxes are mounted at each end of the detector modules. A FE box is the smallest independent readout unit of the OT: the digitized data of the 128 channels of one module are sent via an optical link and received by the TELL1 board. High- and low-voltage, as well as fast- and slow-control signals are connected to each FE box individually. In total, 432 FE boxes are used to read out the OT detector.

This paper describes the detector performance in the first LHC running period from 2010 to 2012, when the LHCb experiment collected data at stable conditions, corresponding to a typical instantaneous luminosity of about  $3.5 (4.0) \times 10^{32} \text{ cm}^{-2}\text{s}^{-1}$  in 2011 (2012), with a 50 ns bunch crossing scheme and a proton beam energy of 3.5 (4) TeV. The higher instantaneous luminosity, and only half of all bunches being filled, translates into a four times larger occupancy per event as compared to the conditions that correspond to the design parameters.

In Sec. 2 the performance of the services is described in terms of the gas quality, and the low and high voltage stability. In Sec. 3 the performance of the electronics readout is discussed, in particular the noise, amplifier threshold uniformity and time-linearity. The drift-time calibration and position alignment is shown in Sec. 4. The final detector performance in terms of occupancy, single hit efficiency, resolution and radiation hardness is given in Sec. 5.

## 2 Services performance

### 2.1 Gas system

The counting gas for the straw tube detectors of the OT was originally chosen as an admixture of Ar/CO<sub>2</sub>/CF<sub>4</sub>. Studies on radiation resistance first suggested to operate without CF<sub>4</sub> [10], and subsequently with the addition of O<sub>2</sub> [11], leading to the final mixture Ar/CO<sub>2</sub>/O<sub>2</sub> (70/28.5/1.5). This choice is based on the requirement to achieve a reasonably fast charge collection to cope with the maximum bunch crossing rate of 40 MHz at the LHC, a good spatial resolution and to maximize the lifetime of the detectors.

The gas is supplied by a gas system [12] operated in an open mode, without recycling of the gas. The gas system is a modular system, with the mixing module on the surface

	typical values	specifications
Gas flow	800 - 850 l/h	< 1000 l/h
Overpressure in detector	1.6 mbar	< 5 mbar
Impurity (H <sub>2</sub> O content)	< 10 ppm	< 50 ppm

Table 1: Main parameters of the OT gas system.

and two distribution modules, a pump module, an exhaust module and an analysis module in the underground area behind the shielding wall to allow access during beam operation. The gas is split between two distribution modules, each supplying a detector half using 36 individual gas lines. For each gas line the input flow can be adjusted and is measured continuously, as well as the output flow. Each distribution module regulates the pressure in the detector modules. The analysis module allows to sample each of the 36 lines individually at the detector inlet and outlet. An oxygen sensor and a humidity sensor are connected to the analysis rack. The measurement of one gas line takes a few minutes such that each line is measured approximately once every two hours.

The main operational parameters of the gas system are shown in Table 1. The gas flow is kept low to prevent ageing effects observed in laboratory measurements (see Sec. 5.6). The detector modules have been tested to be sufficiently gas-tight, on average below  $1.25 \times 10^{-4}$  l/s (corresponding to 5% gas loss every 2 hours) [13], to prevent the accumulation of impurities from the environment. The level of impurities is monitored by measuring the water content in the counting gas, which is at a level below 10 ppm.

A system with pre-mixed bottles containing in total about  $100 \text{ m}^3$  of Ar/CO<sub>2</sub>/O<sub>2</sub>, is automatically activated in case of electrical power failures of the main gas system, ensuring a uninterrupted flow through the detector at all times. The gas mixture, and the level of impurities (H<sub>2</sub>O) were stable during the whole operation from 2010 to 2012.

## 2.2 Gas monitoring

The gas quality for the OT is crucial, as it directly affects the detector gain and stability, and potentially the hit efficiency and drift-time calibration. Moreover, a wrong gas mixture can lead to accelerated radiation damage or dangerously large currents. The gas gain is determined with the help of two custom built OT modules, of 1 m length, which are irradiated by a <sup>55</sup>Fe source.

One of the monitoring modules that was used in 2011 was constructed using a par-

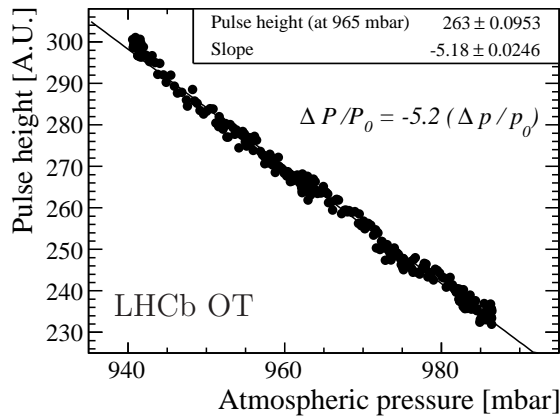


Figure 3: Pressure calibration curve of the <sup>55</sup>Fe spectrum, obtained from the dependence of the pulse height  $P$  as a function of atmospheric pressure  $p$ .



ticular glue, Trabond 2115, that does not provoke gain loss after long-term irradiation with the  $^{55}\text{Fe}$  source. The other module was built with the glue used in mass production, Araldite AY103-1. The modules were half-width modules containing 32 straw tubes. The readout electronics consists of a high voltage board carrying a number of single-channel charge pre-amplifiers.

The  $^{55}\text{Mn}$  K- $\alpha$  line of the  $^{55}\text{Fe}$  source has an energy of 5.9 keV which is used as calibration reference. Two  $^{55}\text{Fe}$  sources with low intensity were used, resulting in a few events per second for both modules. The data acquisition system is based on a multi-functional readout box containing two fast ADC inputs to which the amplified signals are fed. In addition the atmospheric pressure is recorded. The  $^{55}\text{Fe}$  pulses are integrated over 15 minutes, and subsequently analyzed. A double Gaussian distribution is fitted to the  $^{55}\text{Fe}$  spectrum. The peak position is then corrected for the atmospheric pressure.

The pressure is measured inside a buffer volume at the chambers input. The pressure correction is determined from a linear fit to the mean pulse-height as a function of the absolute atmospheric pressure, see Fig. 3. The resulting stability of the gas gain is within  $\pm 2\%$  over 10 days. However, the gain loss due to ageing of the monitoring modules was about 5% over a period of about two months. The monitoring modules were therefore replaced at the end of 2011 by stainless steel modules, sealed with O-rings (instead of the standard construction with Rohacell panels with carbon-fiber facing, glued together to ensure the gas-tightness). The measurements of the gas gain were stable throughout the entire running period of 2012.

## 2.3 Low voltage

The function of the low voltage (LV) distribution system is to provide the bias voltages to the front-end electronics. Each FE box (the GOL/AUX board) hosts three radiation-hard linear voltage regulators (+2.5 V, +3 V and -3 V) biased by two main lines, +6 V and -6 V. Two distribution boxes per C-frame split the +6 V and -6 V supply lines to the 18 FE boxes at the top and the 18 FE boxes at the bottom; all supply lines to the FE boxes are individually provided with slow fuses (4 A for +6 V and 2 A for -6 V) and LED's showing their status.

The low-voltage distribution systems worked reliably throughout the 2010 to 2012 data taking periods. In a few cases a single fuse of a FE box broke and was replaced in short accesses to the LHCb cavern.

## 2.4 High voltage

The anode wires are supplied with +1550 V during operation, which corresponds to a gas gain of about  $5 \times 10^4$  [14]. Each FE box has four independent high voltage (HV) connections, one for each 32-channel HV board. Two mainframes <sup>4</sup>, each equipped with four 28-channels supply boards <sup>5</sup>, are used as HV supply. Using an 8-to-1 distribution

---

<sup>4</sup>CAEN SY1527LC ®.

<sup>5</sup>A1833B PLC ®.

scheme a total of 1680 HV connections of the detector are mapped on 210 CAEN HV channels. The distribution is realized using a patch panel which offers the possibility to disconnect individual HV boards by means of an HV jumper. Both components, the HV supply as well as the patch panel, are located in the counting house. Access to the HV system during data taking is therefore possible.

The typical current drawn by a single HV channel (supplying 256 detector channels) depends on the location in the detector and varies between 20 and  $150\ \mu\text{A}$ . The short-circuit trip value per HV channel was set to  $200\ \mu\text{A}$  with the exception of one channel where the current shows an unstable behaviour, and where the trip value was increased to  $500\ \mu\text{A}$ . The power supply can deliver a maximum current of 3 mA for a single HV channel.

In the 2011 and 2012 running periods there were 8 single detector channels (wires) that showed a short-circuit, either due to mechanical damage, or due to a broken wire. During technical stops these single channels were disconnected, to allow the remaining 31 detector channels on the same HV board to be supplied with high voltage.

### 3 Commissioning and monitoring

Quality assurance tests of the detector modules, the FE-boxes and C-frame services were performed prior to installation. Faulty components were repaired whenever possible. During commissioning and operating phases of the LHCb detector, the stability and the quality of the OT FE-electronics performances was monitored. Upon a special calibration trigger, sent by the readout supervisor, the FE-electronics generates a test-pulse injected via the ASDBLR test input [6, 15]. Test-pulse combinations can be generated, and is implemented such that only even or only odd numbered channels, or all channels simultaneously, are injected with charge.

#### 3.1 Quality assurance of detector modules and C-frame services

The quality of the detector modules was assured by measuring the wire tension, pitch, and leakage current (in air) prior to the module sealing. Subsequently, the gas tightness of the detector module was measured. Finally, the functionality of each wire was validated in the laboratory immediately after production, by measuring the response to radioactive sources ( $^{55}\text{Fe}$  or  $^{90}\text{Sr}$ ) [14].

Before and after shipment of the C-frames from Nikhef to CERN, the equipment of the services were checked, namely the gas tightness of the gas supply lines, the dark currents on the high-voltage cables, the voltage drop on the low-voltage supply cables and the power attenuation of the optical fibers [2, 16].

Following the installation of the modules on the C-frames in the LHCb cavern, the gas tightness of each module was confirmed. The response to  $^{55}\text{Fe}$  of approximately half of the straws was measured again, resulting in 12 noisy channels, 7 dead channels, and 4 straws with a smaller gas flow [16].

All FE-boxes were measured on a dedicated test-stand in the laboratory, and the faulty components were replaced. The tests performed on the test-stand are identical to the tests that are performed regularly during running periods. Three sequences of test runs are provided:

- runs with a random trigger at varying ASDBLR threshold settings to measure the noise rate;
- runs with test-pulse injected at the ASDBLR test input, at varying threshold settings to check the full readout chain for threshold uniformity and cross-talk;
- runs with test-pulse (at fixed threshold) at increasing test-pulse delay settings, to determine the time-linearity.

### 3.2 Noise

The noise scan analysis aims at identifying channels that have an “abnormal” level of noise, which may be due to dark pulses from the detector, bad FE-electronics shielding, or bad grounding. In each channel the fraction of hits is determined for increasing values of the amplifier threshold, triggered randomly. The nominal value of the amplifier threshold is 800 mV, which corresponds to an input charge of about 4 fC.

The typical noise occupancy for 128 channels in one FE box is shown in Fig. 4(a) for increasing amplifier threshold, where the occupancy is defined as the ratio of the number of registered hits in that channel over the total number of triggered events. A noise occupancy at the level of  $10^{-4}$  is observed at nominal threshold, as expected from beam tests [18]. These results are representative for about 98% of all FE boxes in the detector.

An example of a FE box with a few noisy channels is shown in Fig. 4(b), where two groups of about 5 noisy channels are identified. About 2% of the FE boxes exhibited

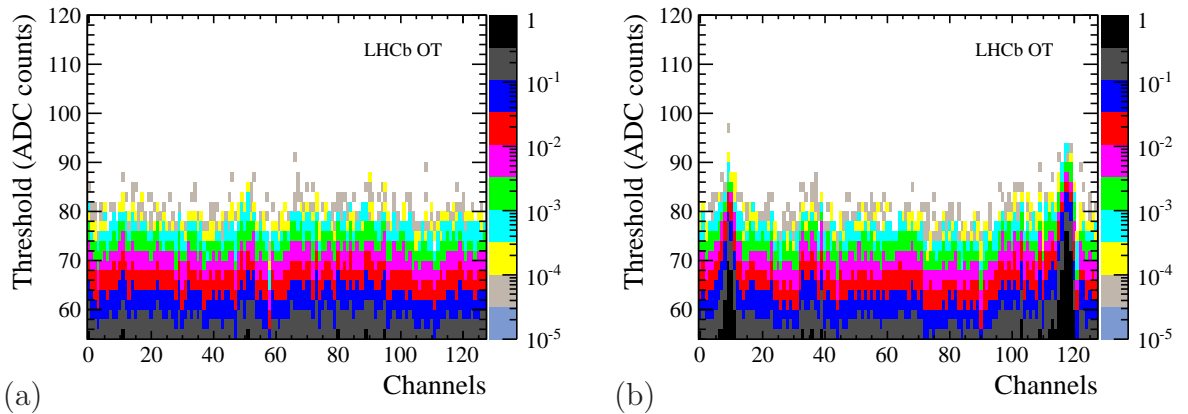


Figure 4: The 2d-hitmap histogram showing the noise occupancy, for each channel, and varying amplifier threshold (1 ADC count  $\approx$  10 mV) [17] for (a) a typical FE-box with good channels and (b) a FE-box with two groups of noisy channels.

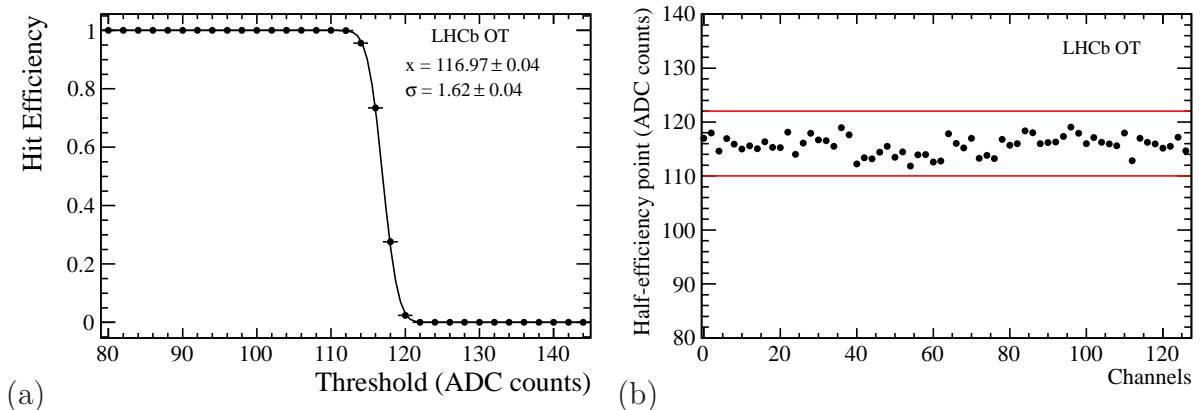


Figure 5: (a) Example of hit-efficiency as function of threshold for a fixed input charge (“high test-pulse”) [17]. (b) Stability of the half-efficiency point for channels in one FE-box (1 ADC count  $\approx$  10 mV).

this noise pattern during the 2011 running period. At the nominal threshold of 800 mV (4 fC) only 0.2% of the channels exhibited a noise occupancy larger than 0.1%. During the 2011/2012 winter shutdown, this noise pattern was understood and identified to be caused by imperfect grounding, and was subsequently solved.

### 3.3 Threshold scans

The threshold scan records hits at fixed input charge (given by either a low or high test-pulse of 4 and 12 fC, respectively) and is aimed at monitoring the gain of the FE-electronics preamplifier, in order to locate dead channels, determine gain deteriorating effects and measure cross-talk.

The ASDBLR chip selection prior to assembly of the FE-box components guarantees a good uniformity of the discriminators, such that a common threshold can be applied for the entire readout without loss of efficiency or increased noise levels [2]. An error function produced by the convolution of a step function (ideal condition in absence of noise) with Gaussian noise, is used to describe the hit-efficiency as a function of the threshold value. The stability of the half-efficiency point for all the channels was studied and the relative variation between channels is expected to be less than  $\pm 60$  mV [2].

An example of the fit to the hit efficiency as a function of amplifier threshold is shown for one channel in Fig. 5(a), and the half-efficiency point for 128 channels in one FE box is shown in Fig. 5(b). Since the start of the data taking period in May 2010 the fraction of fully active channels has been 99.5% or more, see Sec. 5.5.

### 3.4 Delay scans

The delay scan analysis aims at detecting defects in the timing of the OT channels, such as time offsets or non-linearities. An example of the time measurement as a function

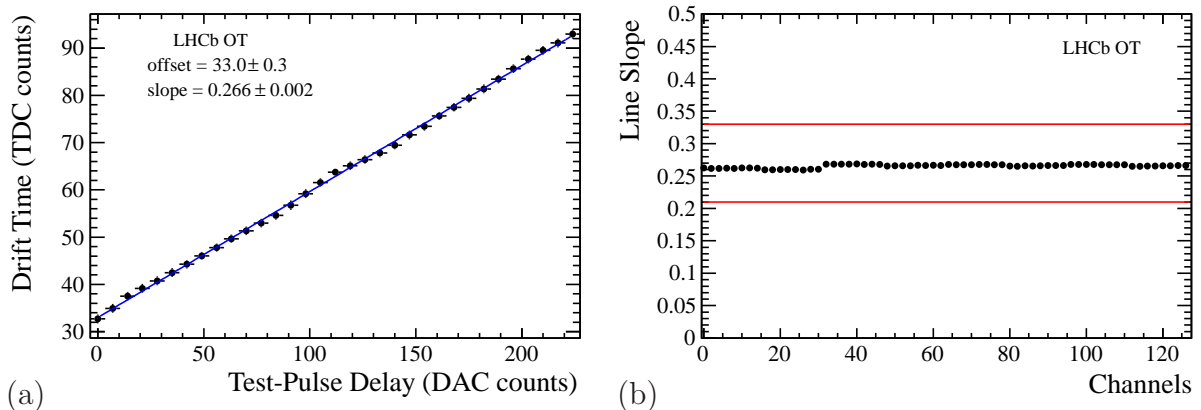


Figure 6: (a) Example of a linear fit of the measured drift-time as a function of the test-pulse delay [17]. The slope corresponds to unity, if both axis are converted to ns (1 DAC count  $\approx 0.1$  ns, while 1 TDC count  $\approx 0.39$  ns). (b) The slope from the linear fit of the timing measurement for all 128 channels in one FE-box.

of the test-pulse delay is shown in Fig. 6(a), where each measurement corresponds to the average of 10,000 time measurements at a given test-pulse delay. The corresponding slope for all 128 channels of one FE box is shown in Fig. 6(b). No anomalous behaviour in the time measurement has been observed. Approximately 96% of all channels have a slope between 0.983 and 1.024 times the average value. Most of the remaining 4% of the channels suffer from insufficient test-pulse stability rather than from pre-amplifier or TDC shortcomings.

## 4 Calibration

The position of the hits in the OT is determined by measuring the drift-time to the wire of the ionisation clusters created in the gas volume. The drift-time measurement can in principle be affected by variations in the time offset in the FE electronics, and is regularly monitored. The spatial position of the OT detector also affects the hit position, and the correct positioning of the detector modules is ensured by periodic alignment campaigns.

### 4.1 Distance drift-time relation

The OT detector measures the arrival time of the ASDBLR signals with respect to the LHC clock,  $T_{\text{clock}}$ , and is referred to as the TDC time,  $t_{\text{TDC}}$ . This time is converted to position information to reconstruct the trajectory of the traversing charged particle, by means of the drift-time–distance relation, or TR-relation. The arrival time of the signal corresponds to the time of the  $pp$  collision,  $T_{\text{collision}}$ , increased by the time-of-flight of the particle,  $t_{\text{tof}}$ , the drift-time  $t_{\text{drift}}$  of the electrons in the straw, the propagation time of the signal along the wire to the readout electronics,  $t_{\text{prop}}$ , and the delay induced by the FE

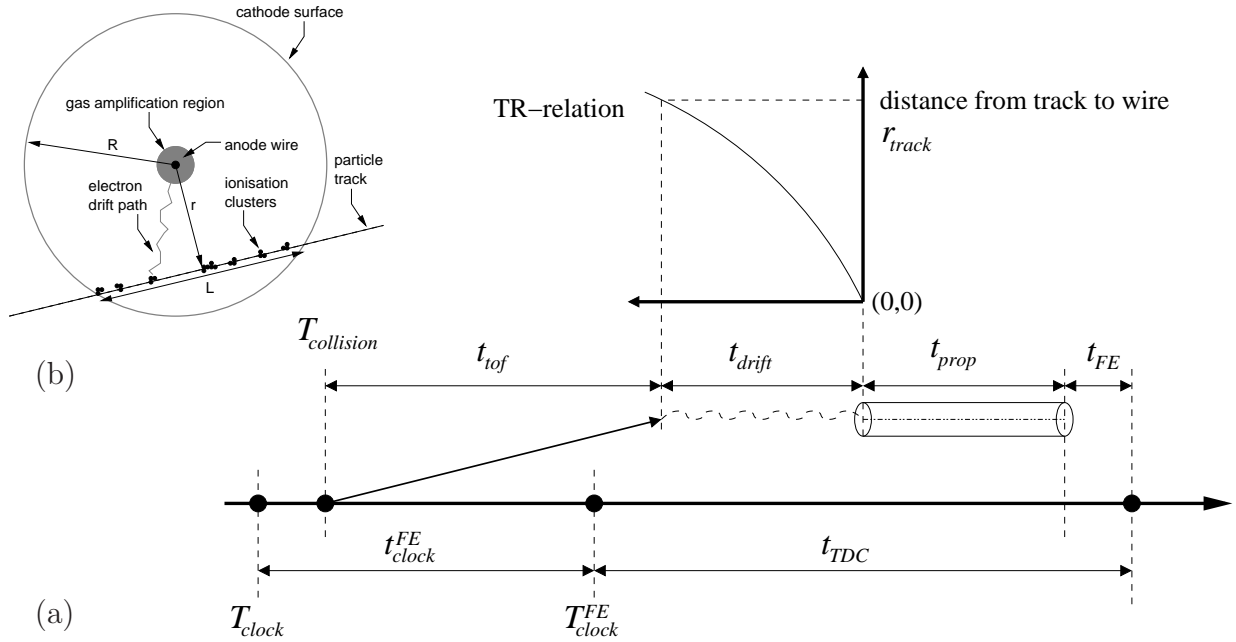


Figure 7: (a) Sketch of the various contributions to the measured TDC time [19], as explained in the text. (b) Picture of a charged particle that traverses a straw.

electronics,  $t_{FE}$ . The various contributions to the TDC time are schematically shown in Fig. 7, and can be expressed as

$$t_{TDC} = (T_{collision} - T_{clock}^{FE}) + t_{tof} + t_{drift} + t_{prop} + t_{FE}. \quad (1)$$

The phase of the clock at the TDC input,  $T_{clock}^{FE}$ , can be adjusted with a shift  $t_{clock}^{FE}$ . The expression for  $t_{TDC}$  can be rewritten as

$$t_{TDC} = (T_{collision} - T_{clock}) + t_0 + t_{tof} + t_{drift} + t_{prop}, \quad (2)$$

where  $t_0 = t_{FE} - t_{clock}^{FE}$ . Variations in  $t_0$  are discussed in the next section. The difference  $t_{clock} = T_{collision} - T_{clock}$  accounts for variations of the phase of the LHC clock received at the LHCb experiment control and is kept below 0.5 ns.

The TR-relation is the relation between the measured drift-time and the closest distance from the particle trajectory to the wire. The TR-relation is calibrated on data by fitting the distribution of drift-time as a function of the reconstructed distance of closest approach between the track and the wire, as shown in Fig. 8(a). At the first iteration the TR-relation obtained from beam tests was used. The line shows the currently used TR-relation [19], which has the following parameterization:

$$t_{drift}(r) = 20.5 \text{ ns} \cdot \frac{|r|}{R} + 14.85 \text{ ns} \cdot \frac{r^2}{R^2}, \quad (3)$$

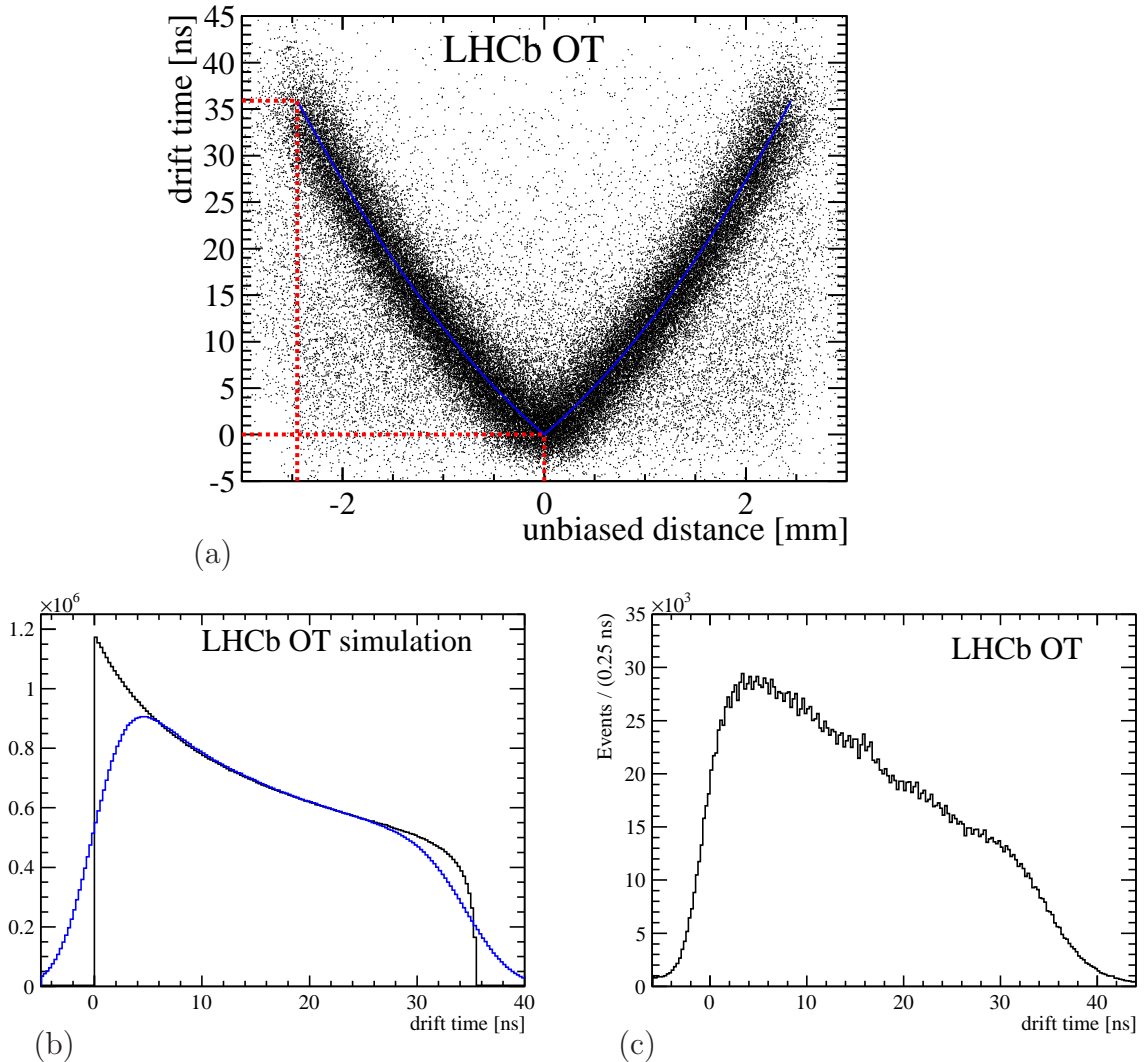


Figure 8: The (a) TR-relation distribution follows the shape of a second order polynomial distribution, which leads to a (b) falling drift-time spectrum (black), which, smeared with the time resolution (blue), leads to the shape of the (c) measured drift-time distribution.

where  $r$  is the closest distance between the track and the wire and  $R = 2.45$  mm is the inner radius of the straw. This TR-relation is compatible with the one obtained from the beam test of 2005 [18],  $t(r) = 20.1 \text{ ns} \cdot \frac{|r|}{R} + 14.4 \text{ ns} \cdot \frac{r^2}{R^2}$ . The maximum drift-time extracted from the parameterization of the TR-relation is 35 ns. Due to the average drift-time resolution of 3 ns, and due to the variation in time-of-flight of the traversing particles, the drift-time distribution broadens, as illustrated in Fig. 8(b). The measured drift-time spectrum after  $t_0$  calibration is shown in Fig. 8(c), and the start of the drift-time spectrum is thus set to 0 ns by construction. During operation, the start of the 75 ns wide readout gate was set to approximately  $-9$  ns, to ensure that also the earliest hits are recorded.

The varying number of entries in the subsequent time bins is a characteristic of the OTIS TDC chip known as the differential non-linearity (caused by variations of the digital delay bin sizes) and does not significantly affect the drift-time resolution [16].

## 4.2 $t_0$ stability

The  $t_{FE}$  values need to be stable to a level better than the time resolution. There are two factors that contribute to the stability of  $t_0$ , usually referred to as the  $t_0$  constants: one is the drift of the global LHCb clock and the second is the drift of FE electronic delays. The first can be extracted from the average over the whole OT of the drift-time residual distribution calculated for every run separately. The second can be estimated from the difference of  $t_0$  values for two different calibrations, for each FE-box.

Figure 9 shows the variation of the LHCb clock as a function of the run number, for the data taking period between May and July 2011. The global LHCb clock is adjusted if it changes by more than 0.5 ns. As a result, the average value of the drift-time residual stays within the range of  $\pm 0.5$  ns.

Figure 10 shows the difference of the  $t_0$  values per FE-box, for two different calibrations performed on runs 89350 and 91933, respectively. These runs correspond to the beginning of two data taking periods in May and July 2011. For most FE boxes the spread of the  $t_0$  constants is smaller than 0.1 ns. The overall shift of 0.4 ns is due to the change of the global LHCb clock. The variation of  $t_0$  is well below the time resolution of 3 ns and does therefore not contribute significantly to the detector resolution.

## 4.3 Geometrical survey

The correct spatial positioning of the OT modules is ensured in three steps. First, the design and construction of the OT detector guarantees a mechanical stability of 100

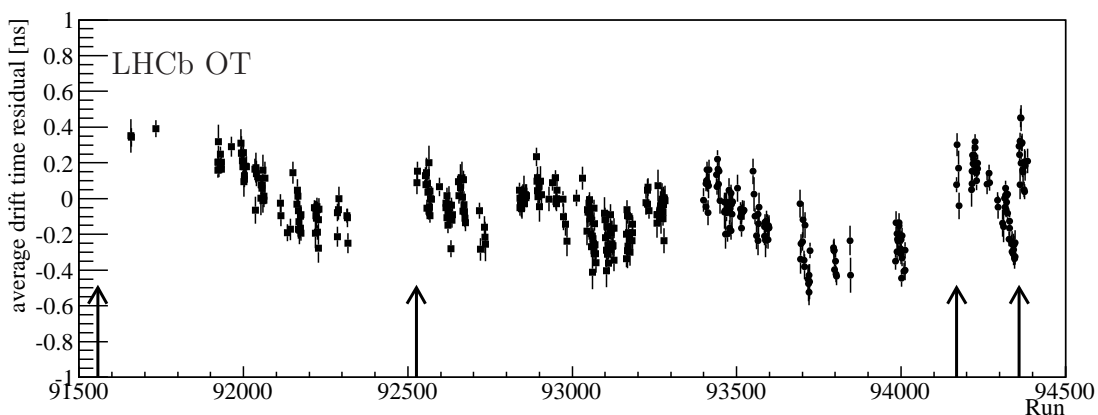


Figure 9:  $t_0$  stability versus run number. Every point corresponds to one run that typically lasts one hour. The arrows indicate the adjustment of the  $t_{clock}$  time.



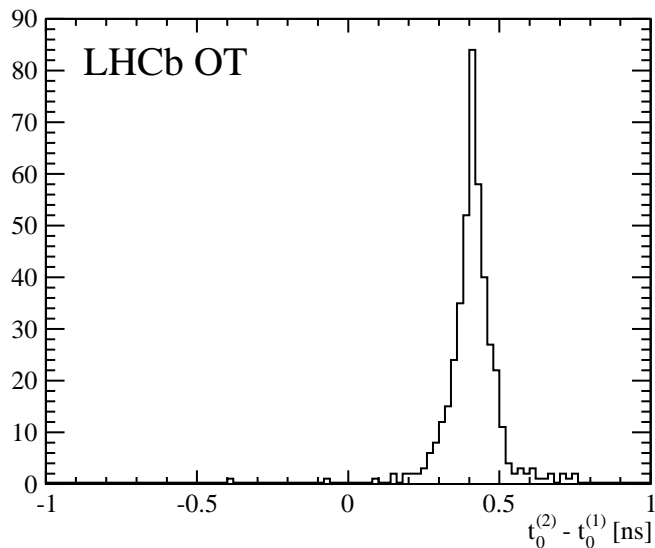


Figure 10: Distribution of differences between  $t_0$  constants per FE box, for two different calibrations. The mean shift originates from a change of the overall  $t_{clock}$  time, whereas the spread shows the stability of the delay  $t_{FE}$  induced by the FE electronics.

(500)  $\mu\text{m}$  in the  $x(z)$  direction. Secondly, an optical survey determined the position of all modules after installation. Finally, the use of reconstructed tracks allows to measure the position of the detector to the highest accuracy.

By construction the anode wire is centered within  $50 \mu\text{m}$  with respect to the straw tube. The detector modules are fixed with dowel-pins to the C-frames at the top and the bottom, with tolerances below  $50 \mu\text{m}$ . The modules are not fixed at the center, making larger variations possible (see Sec. 4.5). Finally, the C-frames are mounted on rails, which fixes the  $z$ -coordinate at the top and at the bottom.

First, the survey confirmed that the rails were straight within the few millimeters tolerance. Then, after installation, the position of the four corners of the C-frames were adjusted until all measured points on the dowel-pins at the top and bottom of the modules, and on the surface at the center of the modules, were within  $\pm 1 \text{ mm}$  of their nominal position. The final survey coordinates provided the corrections to the nominal coordinates of the C-frames and modules [20]. The C-frames can be opened for maintenance, and the reproducibility of the C-frame positioning in the  $x$ -coordinate was checked to be better than the  $200 \mu\text{m}$  precision of the optical survey. The shape of the modules in the  $x$ -coordinate is finally determined using reconstructed tracks, see Sec. 4.5.

#### 4.4 Optical alignment with the Rasnik system

The stability of the C-frame relative position during data taking is monitored by means of the Rasnik system [21, 22]. The Rasnik system consists of a CCD camera that detects a detailed pattern. The pattern, or “mask”, is mounted on the C-frame and a movement

is detected by the CCD camera as a change of the pattern position. All four corners of the 12 C-frames are equipped with a Rasnik system. Together with two additional Rasnik lines to monitor movements of the suspension structure, this leads to a total of 50 Rasnik lines. Due to mechanical conflicts in the installation, only about 2/3 of the lines are used. The intrinsic resolution of the system perpendicular (parallel) to the beam axis is better than 10 (150)  $\mu\text{m}$ . The Rasnik measurements showed that the position of the C-frames is unchanged after opening and closing within  $\pm 10 \mu\text{m}$ , and unchanged within  $\pm 20 \mu\text{m}$  for data taking periods with opposite polarity of the LHCb dipole magnet.

## 4.5 Software alignment

To achieve optimal track parameter resolution the position and orientation of the OT modules must be known with an uncertainty that is negligible compared to the single hit resolution.

The OT C-frames hang on rails and can be moved outside the LHCb acceptance to allow for maintenance work during technical stops of the LHC. Since no survey is performed after such operations, the reproducibility of the nominal position is important. Using track based alignment the reproducibility has been established to be better than 100  $\mu\text{m}$ , consistent with the measurements done with the Rasnik system.

The most precise alignment information is obtained with a software algorithm that uses charged particle trajectories [23]. For each module and C-frame the alignment is parametrized by three translations and three rotations. The algorithm selects high quality tracks and subsequently minimizes the total  $\chi^2$  of those tracks with respect to the alignment parameters. Only a subset of parameters needs to be calibrated to obtain sufficient precision. For the alignment of modules inside each C-frame only the translation in  $x$  and the rotation in the  $xy$  plane are determined. For the C-frames themselves only the translations in  $x$  and  $z$  are calibrated. To constrain redundant degrees of freedom the

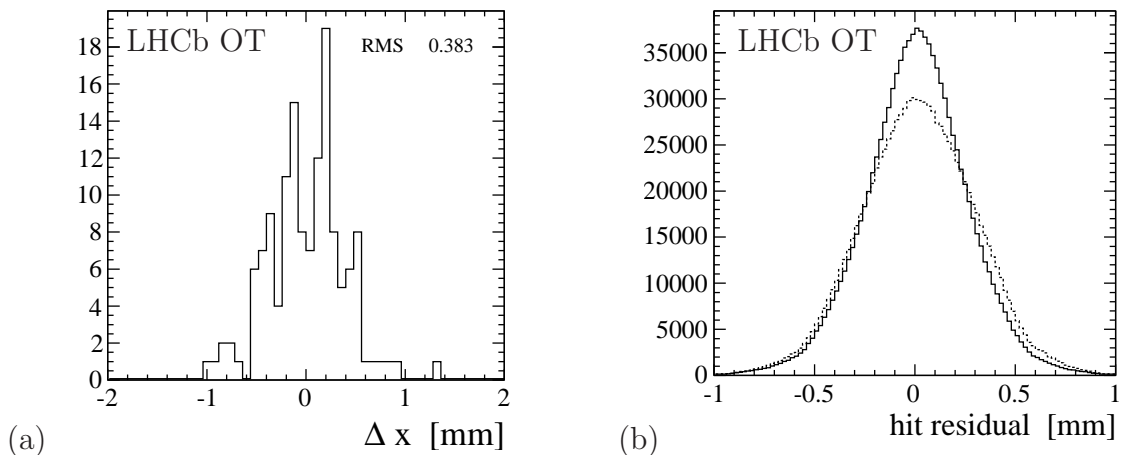


Figure 11: (a) Displacement of modules relative to the survey and (b) hit residuals in the first X-layer of station T2 before (dashed line) and after (continuous line) offline module alignment.

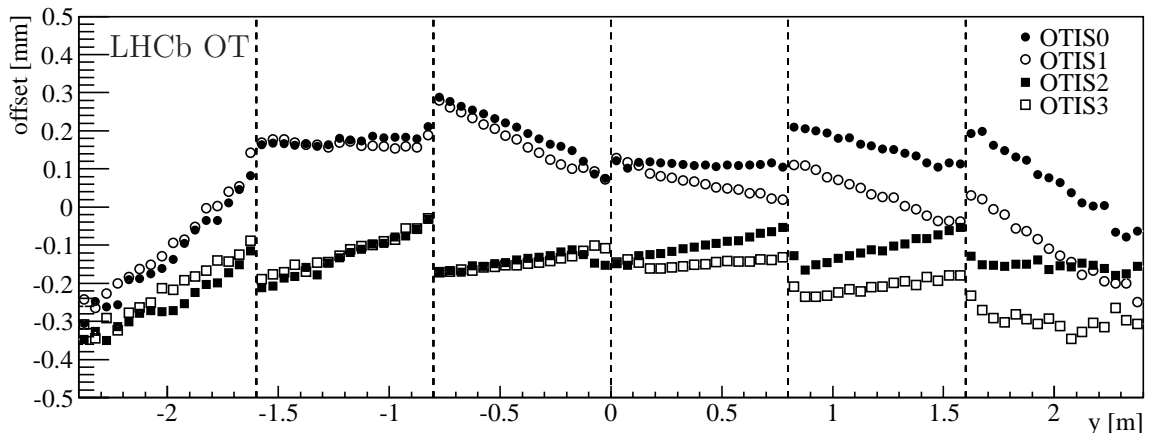


Figure 12: Average hit residual as function of  $y$  coordinate in one particular module (labelled T3L3Q1M7). The four curves show residuals for the four groups of 32 channels within one FE-module. The round markers correspond to one monolayer of 64 straws, whereas the square markers show the residuals of the second monolayer. The vertical dashed lines indicate the position of the wire locators, at every 80 cm along the wire [19].

survey measurements are used as constraints in the alignment procedure.

Figure 11 illustrates the result of an alignment of module positions. For this alignment, tracks were fitted using only the OT hits. At least 18 hits per track were required. To remove poorly constrained degrees of freedom, modules in the first  $x$  and stereo ( $u$ ) layers of stations T1 and T3 were all fixed to their nominal position. Figure 11(a) shows the difference between the  $x$ -position of the module center relative to the survey. Statistical uncertainties in alignment parameters are negligible and the alignment is reproducible in data, taken under similar conditions, within about  $20 \mu\text{m}$ . Figure 11(b) shows the hit residuals in one layer before and after alignment. A clear improvement is observed.

The module displacements in Fig. 11 are larger than expected, based on the expected accuracy of the dowel pins that keep the modules in place. It is assumed that the disagreement can at least partially be explained by degrees of freedom that are not yet corrected for, such as module deformations and the positioning of straws within each module. Figure 12 shows an example of the average hit residual as a function of the coordinate along the wire for one module. A relative displacement of the two monolayers is observed, as well as jumps at the wire locators, which are placed at every 80 cm along the wire length. The effect on the final hit resolution is discussed in Sec. 5.4.

## 5 Performance

The performance of the OT detector was stable in the entire first running period of the LHC between 2010 and 2012, as was shown in the previous sections. No significant failures in the LV, HV and gas systems occurred. The details of the data quality in terms of resolution and efficiency are described below.

### 5.1 Spillover and drift-time spectrum

In order to register all charged particle hits produced in the  $pp$  interaction, three consecutive intervals of 25 ns are readout upon a positive L0-trigger. Only the first hit in the readout window is recorded, as the first hit typically corresponds to the ionization cluster closest to the wire, and it is thus the best estimate for the radial distance to the wire.

In the following, data are studied that are recorded in 75 ns, 50 ns and 25 ns bunch-spacing data taking periods of the LHC. These varying conditions show the effect of so-called spillover hits on the drift-time spectrum and straw occupancies. Distributions obtained in the 75 ns bunch-crossing period are close to those observed with only one single bunch crossing in LHCb, and therefore they will be considered free of spillover.

The drift-time spectrum and the occupancies presented here correspond to events with an average number of visible  $pp$  interactions per bunch crossing of about 1.4, in accordance with the typical run conditions in 2011 and 2012. The events are triggered by any physics trigger, implying that most events contain  $B$  or  $D$ -decays. The drift-time distributions for the 75 ns, 50 ns and 25 ns bunch-spacing conditions are shown in Fig. 13.

The typical drift-time spectrum from the (spillover-free) distribution from the 75 ns running can be understood by inspecting Fig. 8 in Sec. 4.1. The projection of the TR-relation results in a linearly decreasing drift-time spectrum, assuming a flat distribution of the distance between the tracks and the wires. In addition, the number of earlier hits is slightly enhanced in the drift-time distribution, since late hits are hidden by earlier hits on the same straw, as only the first hit is recorded. The recording of the first hit only, induces a “digital dead-time” starting from the first hit until the end of the readout window at 192 TDC counts, or 75 ns. A second source of dead-time originates from the recovery time required by the amplifier. This “analog dead-time” lasts between 8 ns and 20 ns, depending on the signal pulse height, and is usually hidden by the digital dead-time.

The black line in Fig. 13(a) correspond to the data recorded in the 50 ns bunch-spacing period. The contribution from hits from the next bunch-crossing, 50 ns later, is visible between 128 and 192 TDC counts. The relative contribution of these late hits from the next bunch crossing is determined by the average occupancy in the next bunch crossing, and thus depends on the run conditions. In principle it also depends on the occupancy of the triggered event, and thus on the trigger configuration, but in practice that is quite stable. The shape of the drift-time distribution of the late spillover hits corresponds to the nominal, spillover-free (*i.e.* 75 ns) drift-time spectrum, with a shift of +50 ns.

The drift-time shape of the spillover hits from the previous  $-50$  ns bunch-crossing is more complex. It contains the late hits of the drift-time distribution from the previous

bunch-crossing. Naively, the drift-time spectrum of these early hits can be modelled by a shift of the spillover-free distribution by  $-50$  ns, as illustrated by the black line in Fig. 13(b). However, a traversing track can give rise to multiple hits, which are usually not detected due to the digital “dead-time”. These multiple-hits, or “double pulses” from the previous bunch-crossing now become visible, when they fall inside the readout window of the triggered bunch-crossing.

In 30 to 40% of all hits, the first arriving ionization cluster produces a second hit that arrives about 30 ns later. Several effects, such as multiple ionizations, reflections [24] or photon feedback [25], can produce such a double pulse. The time-spectrum of late hits from the previous bunch-crossing, observed in the triggered bunch crossing, is clearly isolated by studying “empty” bunch-crossings with “busy” previous bunch-crossings. The empty and busy bunch-crossings are selected using the total activity in the calorimeter in the subsequent bunch-crossings. The resulting drift-time spectrum of late hits from busy previous bunch-crossings in empty triggered events is shown as the red line in Fig. 13(b). The large number of double-pulses around 40 TDC counts, or 15 ns explains the enhancement of hits between 0 and 25 ns in the 50 ns bunch-crossing drift-time spectrum compared to the spillover-free drift-time spectrum from the 75 ns data, see Fig. 13(a).

Finally, the drift-time spectrum corresponding to the 25 ns bunch spacing conditions (recorded in Dec 2012) is also overlaid in Fig. 13(a). An overall increase of the number of hits is seen for a comparable number of overlapping events, compared to the 50 and 75 ns running conditions.

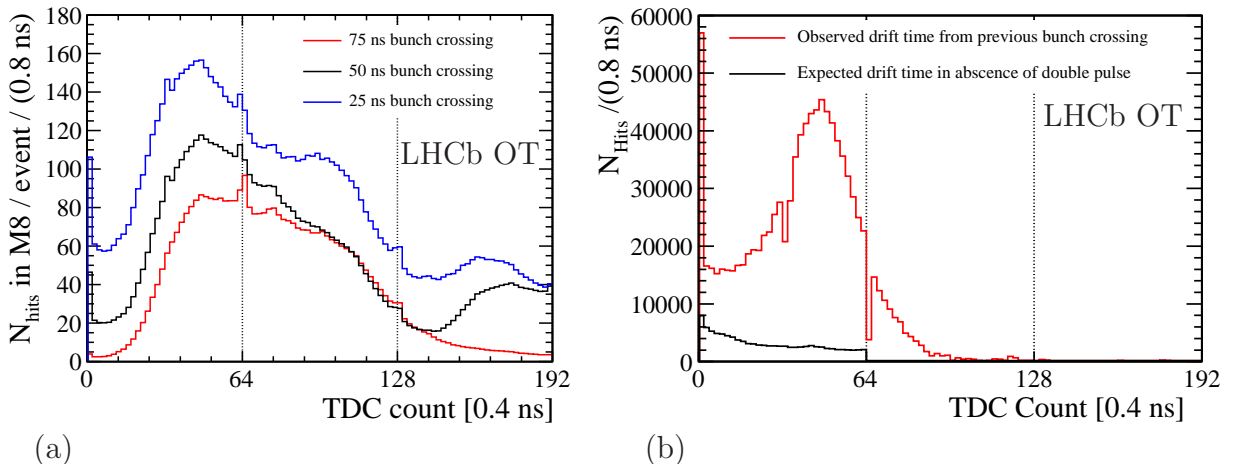


Figure 13: (a) Drift-time distribution in module 8, close to the beam, for 75 ns, 50 ns, 25 ns bunch-crossing spacing in red, black and blue, respectively. The vertical lines at 64 and 128 TDC counts correspond to 25 and 50 ns, respectively. The distributions correspond to all hits in 3000 events for each bunch-crossing spacing, recorded with an average number of overlapping events of  $\mu = 1.2, 1.4$  and  $1.2$ , for 75 ns, 50 ns and 25 ns conditions, respectively. (b) The drift-time distribution for empty events illustrates the contribution from spillover hits from “busy” previous bunch-crossings (red). The naive expectation of the spillover distribution is shown in black, and is obtained by shifting the nominal drift-time spectrum by  $-50$  ns.

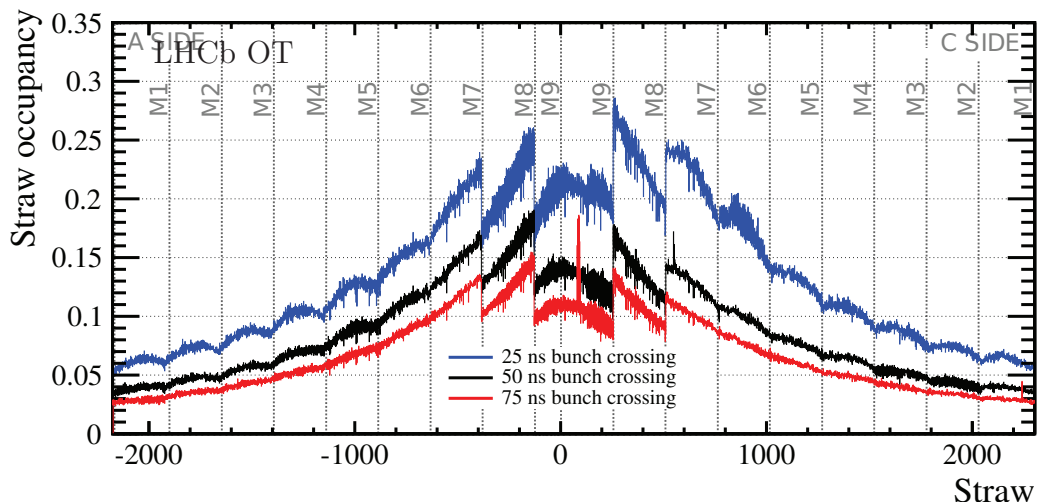


Figure 14: Straw occupancy for 75 ns, 50 ns, 25 ns bunch-crossing spacing in red, black and blue, respectively, for typical run conditions with on average 1.2, 1.4 and 1.2 overlapping events per bunch crossing, respectively. One module contains in total 256 straws, whereas the width of one module is 340 mm. The steps in occupancy at the center of the detector correspond to the location of the shorter S-modules, positioned further from the beam in the  $y$ -coordinate. The data corresponding to 25 ns bunch-crossing spacing, was recorded with opposite LHCb-dipole polarity, as compared to the other two data sets shown here.

## 5.2 Occupancy

The occupancy per straw is shown in Fig. 14 for typical run conditions in 2011 and 2012, triggered by any physics trigger. The occupancy is shown for events with 25, 50 and 75 ns bunch-crossing conditions. In absence of spillover (*i.e.* the 75 ns case), the occupancy varies from about 15% in the innermost modules to about 3% in the outermost modules. For the data taken with 50 ns bunch-crossing spacing, about 30% of all hits originate from spillover, *i.e.* from the previous bunch crossing.

Monte Carlo simulations demonstrate that most of the hits originate from secondary charged particles, produced in interactions with material. Figure 15 shows the fraction of hits that originate from a particle created at a given  $z$  coordinate. The hits from tracks that originate from the genuine  $pp$  interaction or a subsequent particle decay, are predominantly located close to the interaction region. They represent 27.7% (resp. 27.1% and 25.7%) of all hits seen in station T1 (resp. T2 and T3). The remaining hits originate from charged particles created in secondary interactions, mainly in the support of the beam pipe situated in the magnet or in the detectors located upstream of the detector layer (Vertex Locator, Ring Imaging Detector, Tracker Turicensis (TT), Inner Tracker (IT) and OT).

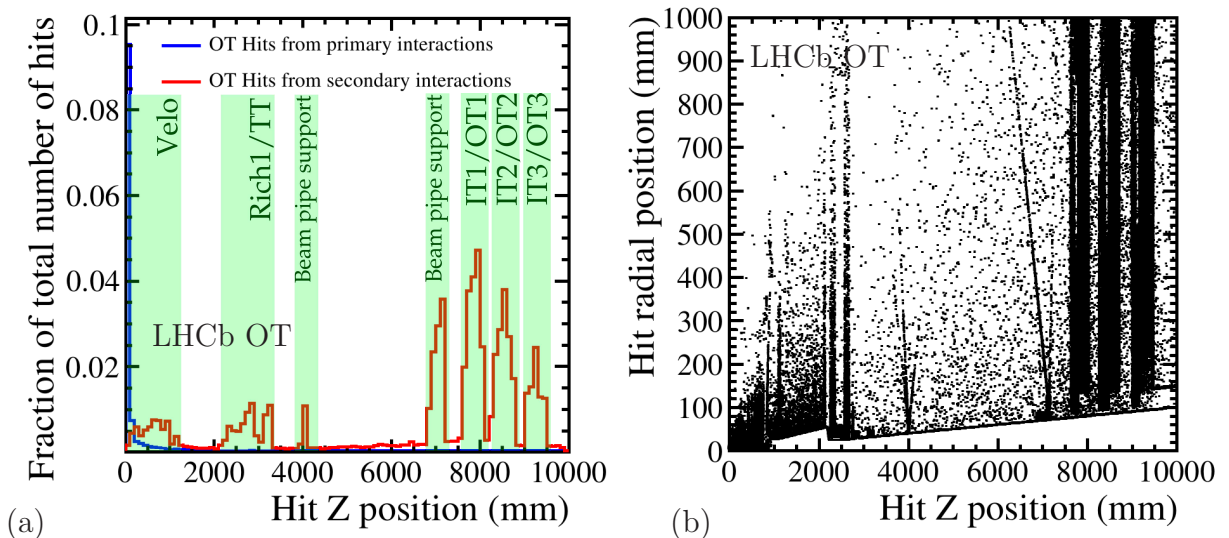


Figure 15: Coordinate of the origin of charged particles that produce a hit in the OT detector. (a) The blue histogram peaks at  $z = 0$  and corresponds to hits from particles produced at the  $pp$  interaction point and their daughters, while the hits from particles produced in secondary interactions (red) predominantly originate from  $z > 0$ . (b) The longitudinal and transverse position of the origin of charged particles produced in secondary interactions, showing the structure corresponding to the material in the detector.

### 5.3 Hit efficiency

A high single-hit efficiency is crucial, as it affects the tracking efficiency, and eventually the physics performance of the LHCb experiment. The efficiency is defined as the number of observed hits in a particular detector region over the number of expected hits in the same region. The number of expected hits is estimated by considering charged particle tracks in  $pp$  collision data and extrapolating the charged particle trajectory to the monolayer under study.

In order to determine the hit efficiency, good quality tracks have been selected, requiring a  $\chi^2/ndf$  (where  $ndf$  are the number of degrees of freedom) less than 2 and a minimum number of 21 hits in the OT detector. This corresponds to accepting about 87% of all good tracks. For each track, every OT monolayer has been considered, and a hit has been searched in the straw closest to the charged particle trajectory. Since a track is reconstructed by the same hits that are subsequently used for the efficiency estimation, the large number of required hits could bias the efficiency determination. This has been corrected for by not considering the monolayer under study, when counting the minimum number of hits per track.

The hit efficiency is studied as a function of the distance between the predicted track position and the center of the considered straw. The resulting single-hit-efficiency profile is shown in Fig. 16(a), summed for all straws in the long modules closest to the beam-pipe (module 7).

The shape of the efficiency profile can be understood by considering two effects. Near

the straw tube edge, the path length of ionizing particles inside the gas volume is limited, resulting in a sizeable probability for not ionizing the gas. This can be described with a Poissonian distribution for the single-hit probability. Secondly, the finite track resolution smears the distribution at the edge of the straw tube, lowering the efficiency inside and increasing the efficiency outside of the straw. The finite probability to detect a hit outside straw tube originates from random hits unrelated to the track under study, and is proportional to the average occupancy in that part of the detector.

The straw tube profile can thus be fitted with the following line shape, which describes the efficiency as a function of the distance  $r$  from the center of the straw,

$$p(r) = 1 - \left(1 - \varepsilon(r) \otimes \text{Gauss}(r|0, \sigma)\right) \cdot (1 - \omega), \quad (4)$$

$$\text{with } \varepsilon(r) = \varepsilon_0 \left(1 - e^{-\frac{2\sqrt{R^2 - r^2}}{\lambda}}\right),$$

where  $R = 2.45$  mm is the inner radius of the straw,  $\omega$  is the average occupancy,  $\lambda$  is the effective ionization length of a charged particle in the gas volume, and  $\sigma$  is the track resolution.

The deviation from the perfect efficiency is quantified in Eq. (4) by  $\varepsilon_0$ . However, in the following, an operationally straightforward definition of the single-hit efficiency is used. The single-hit efficiency per straw is defined as the average hit efficiency  $\varepsilon_{hit}$  in the limited range close to the wire,  $|r| < 1.25$  mm. The inefficient regions between two straws lead to the maximum efficiency of 93%, integrated over the monolayer, and is calculated by taking the ratio of the straw diameter of 4.9 mm over the pitch, 5.25 mm. The inefficient

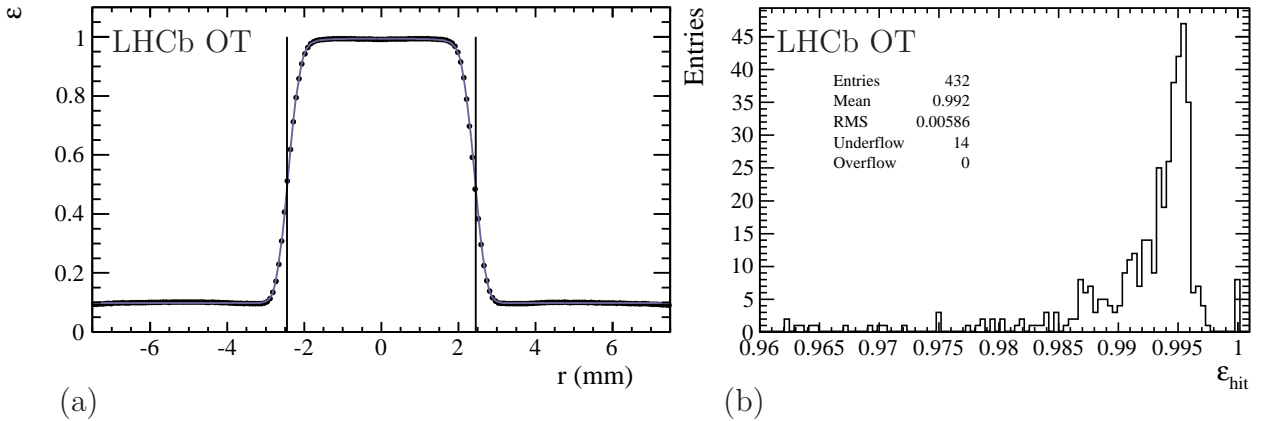


Figure 16: (a) Efficiency profile as a function of the distance between the predicted track position and the center of the straw, for straws in the long F-modules closest to the beampipe (module 7). The vertical lines represent the straw tube edge at  $|r| = 2.45$  mm. (b) Histogram of the average efficiencies per half module (128 channels), at the center of the straw,  $|r| < 1.25$  mm, for runs 96753, 96763 and 96768 on 22 July 2011.



regions are covered by the neighbouring monolayer in the same module, which is staggered by half a straw pitch.

A fit to the straw efficiency profile, using Eq. (4), separately for the profiles of the nine module positions, yields the following average parameters,  $\langle\lambda\rangle = 0.79 \pm 0.09$  mm,  $\langle\varepsilon_0\rangle = 0.993 \pm 0.003$ ,  $\langle\sigma\rangle = 0.26 \pm 0.06$  mm,  $\langle\omega\rangle = 0.07 \pm 0.02$ , where the quoted uncertainty is the standard deviation from the values obtained for the nine different module positions. Note that these parameters are averaged over the different module positions, corresponding to different conditions. For example, the measured occupancy  $\omega$  varies from 4.7% to 9.7% depending on the distance of the module to the beam. Fits to the single-hit efficiency profiles show that the efficiency is close to maximal, *i.e.* the value for  $\varepsilon_0$  is consistent with unity.

For each half-module, corresponding to one FE box, the average single-hit efficiency  $\varepsilon_{hit}$  has been calculated and the result is shown in Fig. 16(b). The efficiency distribution peaks around 99.5%, consistent with the measurements from beam tests [18]. The average of the distribution is about 99.2%. This value is consistent with the fit to the straw tube profile, shown in Fig. 16(a). The large hit efficiency is a prerequisite for large efficiency to reconstruct charged particle's tracks in LHCb. The average tracking efficiency is approximately 95% in the region covered by the LHCb detector [26].

The modules that are located at the edge of the geometrical acceptance of LHCb, in particular the outermost modules in the first station, detect a relatively small number of tracks. All eight FE boxes in Fig. 16(b) with a value of the efficiency exactly equal to 1, and 11 out of the 14 FE boxes with  $\varepsilon_{hit} < 96\%$ , are attached to modules located most distant from the beampipe (module 1), and suffer from few tracks in the efficiency determination. The remaining three FE boxes with  $\varepsilon_{hit} < 96\%$  suffer from hardware problems, representing  $3/432 = 0.7\%$  of all FE boxes.

In order to calculate the average efficiency for each module position, modules with few

Table 2: Average single-hit efficiencies  $\varepsilon_{hit}$  near the center of the straws,  $|r| < 1.25$  mm, for different module positions of the OT detector.

Module position	Efficiency (%)
1	$98.085 \pm 0.011$
2	$99.130 \pm 0.005$
3	$99.279 \pm 0.003$
4	$99.277 \pm 0.003$
5	$99.282 \pm 0.002$
6	$99.342 \pm 0.002$
7	$99.286 \pm 0.002$
8	$99.200 \pm 0.002$
9	$99.351 \pm 0.003$

tracks, ie. with an efficiency lower than 96%, or with an efficiency equal to unity, have been discarded. The average efficiency thus obtained for each module position is listed in Table 2 where the reported uncertainties are statistical.

As shown above, the decrease of the hit efficiency close to straw edge is partially due to the fact that the charged particle traverses a short distance through the straw volume. Hence, the probability to not form an ionization cluster increases towards the straw edge. Alternatively, the effective ionization length  $\lambda$  can be probed by selecting only those tracks that pass *close* to the wire. In contrast to the first method exploiting Eq. 4, here the determination of the ionization length is *not* affected by absorption of drifting electrons. The larger the ionization length, the more hits will exhibit a *large* drift-time, as the ionization does not necessarily occur close to the wire. The effective ionization length  $\lambda$  extracted from particles traversing the straw within  $|r| < 0.1$  mm amounts to about 0.7 mm [19, 27], consistent with  $0.79 \pm 0.09$  mm, as obtained above.

## 5.4 Hit resolution

The single hit resolution is determined using good quality tracks, selected by requiring a momentum larger than 10 GeV, at least 16 OT hits and a track-fit  $\chi^2/ndf < 2$  (excluding the hit under study, and excluding any hit in the neighbouring monolayer in the same module). For a given track, the drift-time and the hit position in a straw are predicted, and compared with the measured drift-time and position, respectively. The resulting distribution of the drift-time residuals and hit position residuals are shown in Fig. 17.

The drift-time residual distribution has a width of 3 ns which is dominated by the ionization and drift properties in the counting gas. The granularity of the step size of the TDC of 0.4 ns has a negligible impact on the drift-time resolution. The hits in the left tail

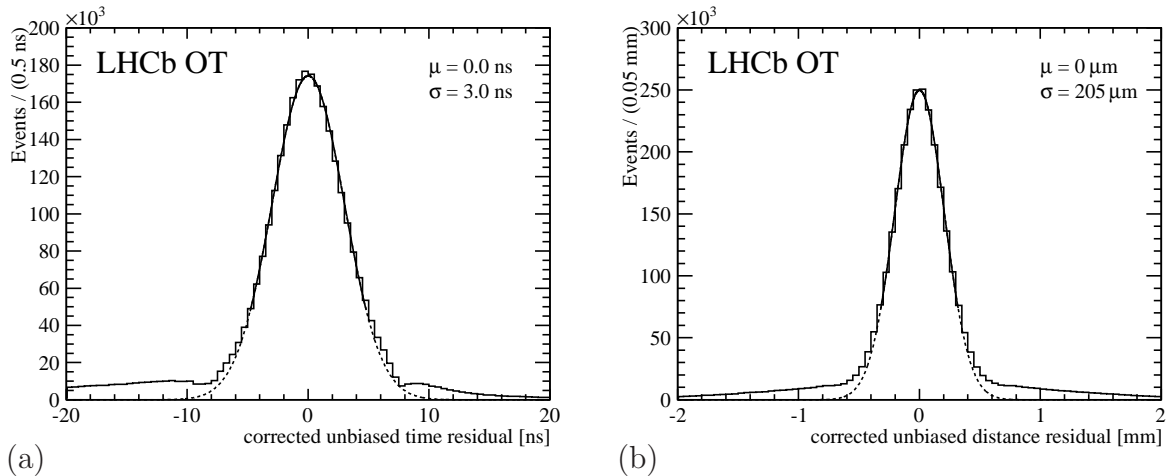


Figure 17: (a) Drift-time residual distribution and (b) hit distance residual distribution [19]. The core of the distributions (within  $\pm 1\sigma$ ) are fitted with a Gaussian function and the result is indicated in the figures.

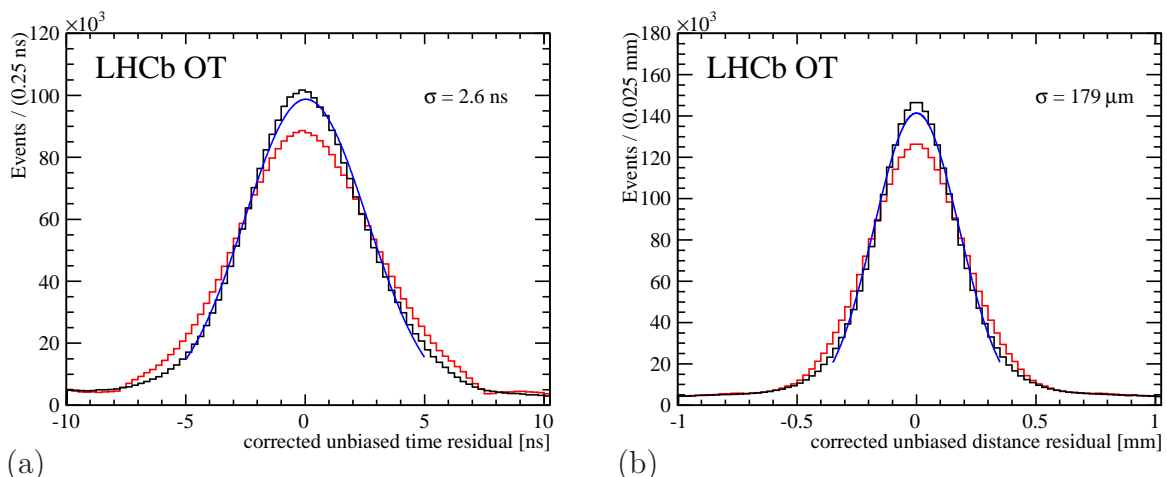


Figure 18: Improvement in (a) drift-time residual distribution and (b) hit distance residual distribution, (red) before and (blue) after allowing for a different horizontal displacement per half monolayer, corresponding to 64 straws [19].

of the drift-time residual distribution are early hits, that do not originate from the track under study, but instead are a combination of noise hits, hits from different tracks in the same bunch crossing, and hits from tracks from previous bunch crossings (spill-over hits).

The hit distance residual distribution has a width of about  $205 \mu\text{m}$ , which is close to the design value of  $200 \mu\text{m}$ . An improvement of the hit position resolution is foreseen when the two monolayers within one detector module are allowed to be relatively displaced to each other in the global LHCb alignment procedure. By allowing a different average horizontal displacement per half monolayer, containing 64 straws, a single hit resolution of approximately  $180 \mu\text{m}$  is in reach, see Fig. 18. Also allowing for a rotation of each half monolayer, improves the single hit resolution further to  $160 \mu\text{m}$ . These values refer to a Gaussian width of the resolution, determined from a fit to the residual distribution, within two standard deviations of the mean. This is in good agreement with the hit resolution below  $200 \mu\text{m}$ , as obtained in beam tests [18].

## 5.5 Monitoring of faulty channels

Noisy or dead channels due to malfunctioning front-end electronics are timely identified through the analysis of the calibration runs as described in Sec. 3. With the full offline data set available, the performance of individual channels is also monitored by comparing the occupancy to the expected value. First, the performance of entire groups of 32 channels is verified. Then, within a group of 32 channels, the occupancy is compared to the truncated mean, after correcting for the dependence of the occupancy on the distance to the beam. If the occupancy is above (below) 6 standard deviations from the truncated mean, the channel is declared “noisy” (“dead”). For a typical run recorded at the end of 2012 (run 133785), when all front-end modules were functioning properly, the OT contained 52 dead channels and 8 noisy channels, evenly distributed over the detector. The evolution

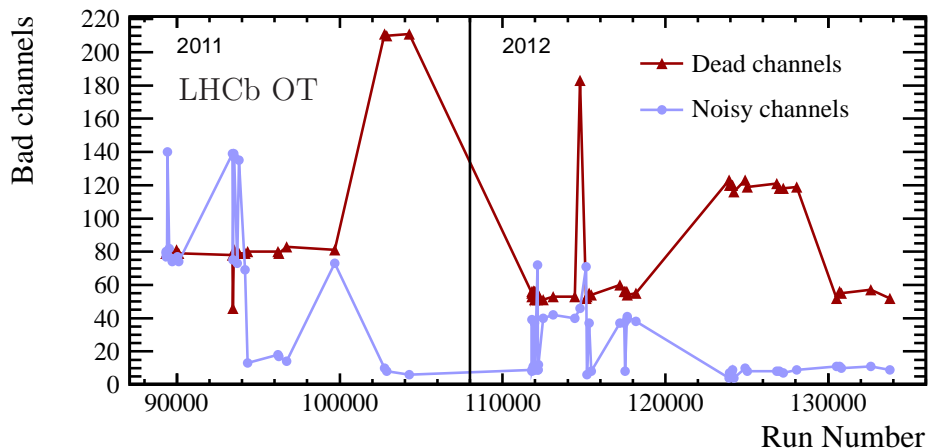


Figure 19: The evolution of number of dead and noisy channels as function of run number in the 2011 and 2012 running periods. The definition of dead and noisy channels is given in the text. The three periods with larger number of dead channels, correspond to periods with a problem affecting one entire front-end box.

of the number of bad channels throughout the 2011 and 2012 running periods is shown in Fig. 19.<sup>6</sup>

## 5.6 Radiation tolerance

It was discovered that, in contrast to the excellent results of extensive ageing tests in the R&D phase, final production modules suffered from gain loss after moderate irradiation (i.e. moderate collected charge per unit time) in laboratory conditions. The origin of the gain loss was traced to the formation of an insulating layer on the anode wire [11], that contains carbon and is caused by outgassing inside the gas volume of the plastifier contained in the glue [28]. Remarkably, the gain loss was only observed upstream of the source position with respect to the gas flow.

A negative correlation was observed between the ageing rate and the production of ozone [11], which suggests that the gain loss is prevented under and downstream of the source due to the formation of ozone in the avalanche region. As a consequence it was decided to add 1.5% O<sub>2</sub> to the original gas mixture of Ar/CO<sub>2</sub>, to mitigate possible gain loss. In addition, a beneficial effect from large induced currents was observed, which removed the insulating layers from irradiation in the laboratory. These large currents can either be invoked by large values of the high voltage in the discharge regime (dark currents), or by irradiating the detector with a radioactive source [28].

No signs of gain loss have been observed in the 2010 to 2012 data taking period of LHCb, corresponding to a total delivered luminosity of 3.5 fb<sup>-1</sup>. Most of the luminosity

<sup>6</sup>The three periods with larger number of dead channels correspond to a broken laser diode (VCSEL) between September and December 2011 at location T1L3Q0M2, a broken fuse in May 2012 at location T3L3Q0M8, and desynchronization problems between July and September 2012 at location T2L2Q0M9. Note that the front-end box at location M9 on the C-side reads out only 64 straws.

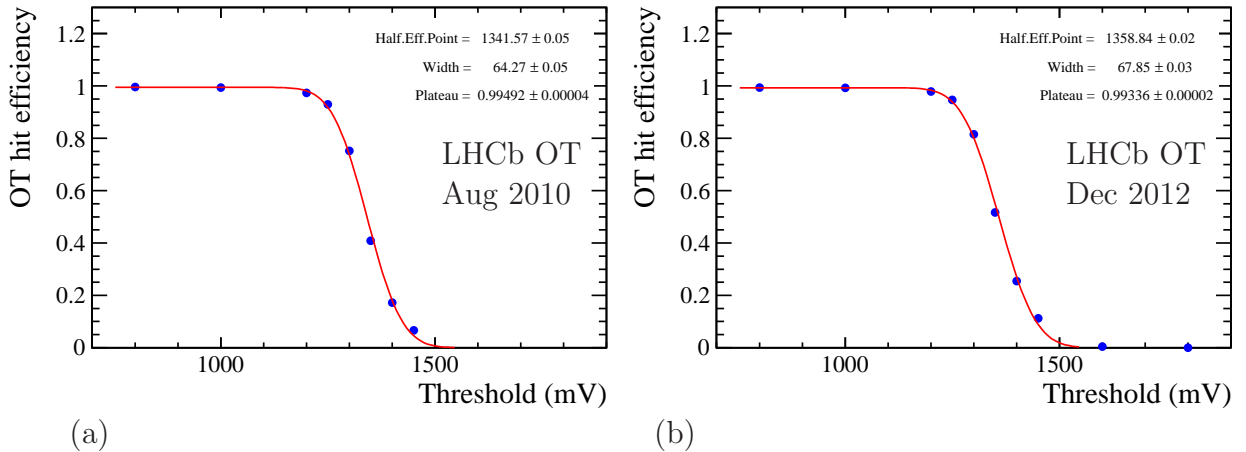


Figure 20: Hit efficiency as a function of amplifier threshold in (a) August 2010 and (b) December 2012 for the inner region, defined as  $\pm 60$  cm in  $x$  and  $\pm 60$  cm in  $y$  from the central beam pipe, summed over all OT layers. Note that the threshold value of 1350 mV, where the efficiency is 50%, is much higher than the operational threshold of 800 mV, and is equivalent to multiple times the corresponding average hit charge.

was recorded in 2011 and 2012, corresponding to about  $10^7$  s of running at an average instantaneous luminosity of  $3.5 \times 10^{32} \text{ cm}^{-2} \text{ s}^{-1}$ , and the region closest to the beam accumulated an integrated dose equivalent to a collected charge of 0.12 C/cm. Possible changes in the gain are studied by increasing the amplifier threshold value during LHC operation, and comparing the value where the hit efficiency drops, see Fig. 20. This value of the amplifier threshold can be converted to hit charge, which provides information on the change of the detector gain. This method to measure the gain variations is outlined in detail in Ref. [29].

## 6 Conclusions

The Outer Tracker has been operating in the 2010, 2011 and 2012 running periods of the LHC without significant hardware failures. The low voltage, high voltage and gas systems showed a reliable and stable performance. Typically 250 channels out of a total of 53,760 channels were malfunctioning, resulting in 99.5% working channels. The missing channels were mainly caused by problems in the readout electronics, whereas only a handful channels could not stand the high voltage on the detector.

The occupancy of the Outer Tracker detector of typically 10% was larger than anticipated, due to twice larger instantaneous luminosity at LHCb with half the number of bunches in the LHC, compared to the design specifications. Despite these challenging conditions, the Outer Tracker showed an excellent performance with a single-hit efficiency of about 99.2% near the center of the straw, and a single hit resolution of about  $200 \mu\text{m}$ . No signs of irradiation damage have been observed.

## Acknowledgements

We wish to thank our colleagues of the CERN Gas Group for their continuous support of the Outer Tracker gas system. We also express our gratitude to our colleagues in the CERN accelerator departments for the excellent performance of the LHC. We thank the technical and administrative staff at the LHCb institutes. We acknowledge support from CERN and from the national agencies: CAPES, CNPq, FAPERJ and FINEP (Brazil); NSFC (China); CNRS/IN2P3 and Region Auvergne (France); BMBF, DFG, HGF and MPG (Germany); SFI (Ireland); INFN (Italy); FOM and NWO (The Netherlands); SCSR (Poland); MEN/IFA (Romania); MinES, Rosatom, RFBR and NRC “Kurchatov Institute” (Russia); MinECo, XuntaGal and GENCAT (Spain); SNSF and SER (Switzerland); NAS Ukraine (Ukraine); STFC (United Kingdom); NSF (USA). We also acknowledge the support received from the ERC under FP7. The Tier1 computing centres are supported by IN2P3 (France), KIT and BMBF (Germany), INFN (Italy), NWO and SURF (The Netherlands), PIC (Spain), GridPP (United Kingdom). We are thankful for the computing resources put at our disposal by Yandex LLC (Russia), as well as to the communities behind the multiple open source software packages that we depend on.

## References

- [1] LHCb collaboration, A. A. Alves Jr. *et al.*, *The LHCb detector at the LHC*, JINST **3** (2008) S08005.
- [2] E. Simioni, *New physics from rare beauty*, PhD thesis, Vrije Universiteit, Amsterdam, 2010, CERN-THESIS-2010-031.
- [3] LHCb collaboration, P. Barbosa *et al.*, *Outer Tracker technical design report*, , CERN-LHCC-2001-024.
- [4] A. Berkien *et al.*, *The LHCb outer tracker front end electronics*, CERN-LHCB-2005-025.
- [5] G. Haefeli *et al.*, *The LHCb DAQ interface board TELL1*, Nucl. Instrum. Meth. **A560** (2006) 494.
- [6] N. Dressnandt *et al.*, *Implementation of the ASDBLR and DTMROC ASICS for the ATLAS TRT in DMILL Technology*, 6th Workshop on Electronics for LHC Experiments 2000.
- [7] H. Deppe, U. Stange, U. Trunk, and U. Uwer, *The OTIS reference manual*, CERN-LHCB-2008-010.
- [8] U. Stange, *Development and characterisation of a radiation hard readout chip for the LHCb outer tracker detector*, PhD thesis, University of Heidelberg, 2005, CERN-THESIS.

- [9] U. Uwer *et al.*, *Specifications for the IF13-2 Prototype of the Auxiliary Board for the Outer Tracker*, CERN-LHCB-2005-039.
- [10] S. Bachmann *et al.*, *The straw tube technology for the LHCb outer tracking system*, Nucl. Instrum. Meth. **A535** (2004) 171.
- [11] S. Bachmann *et al.*, *Ageing in the LHCb outer tracker: Phenomenon, culprit and effect of oxygen*, Nucl. Instrum. Meth. **A617** (2010) 202.
- [12] R. Barillere and S. Haider, *LHC gas control systems: A common approach for the control of the LHC experiments gas systems*, CERN-JCOP-2002-14.
- [13] P. Vankov, *Study of the B-meson lifetime and the performance of the Outer Tracker at LHCb*, PhD thesis, Vrije Universiteit, Amsterdam, 2008, CERN-THESIS-2008-091.
- [14] G. Van Apeldoorn *et al.*, *Outer tracker module production at NIKHEF: Quality assurance*, CERN-LHCB-2004-078.
- [15] V. Gromov and T. Sluijk, *Study of operational properties of the ASDBLR chip for the LHCb Outer Tracker*, CERN-LHCB-2000-054.
- [16] F. Jansen, *Unfolding single-particle efficiencies and the Outer Tracker in LHCb*, PhD thesis, Vrije Universiteit, Amsterdam, 2011, CERN-THESIS-2011-068.
- [17] B. Storaci, *First measurement of the fragmentation fraction ratio  $f_s/f_d$  with tree level hadronic decays at 7 TeV pp collisions*, PhD thesis, Vrije Universiteit, Amsterdam, 2012, CERN-THESIS-2012-111.
- [18] G. van Apeldoorn *et al.*, *Beam tests of final modules and electronics of the LHCb outer tracker in 2005*, CERN-LHCB-2005-076.
- [19] A. Kozlinskiy, *Outer Tracker calibration and open charm production cross section measurement at LHCb*, PhD thesis, Vrije Universiteit, Amsterdam, 2013, CERN-THESIS-2012-338.
- [20] J. Amoraal, *Alignment with Kalman filter fitted tracks and reconstruction of  $B_s^0 \rightarrow J/\psi\phi$  decays*, PhD thesis, Vrije Universiteit, Amsterdam, 2011, CERN-THESIS-2011-011.
- [21] H. Dekker *et al.*, *The RASNIK/CCD 3-dimensional alignment system*, eConf **C930928** (1993) 017, IWAA-1993-017.
- [22] M. Adamus *et al.*, *Test results of the RASNIK optical alignment monitoring system for the LHCb outer tracker detector*, LHCB-2001-004.
- [23] J. Amoraal *et al.*, *Application of vertex and mass constraints in track-based alignment*, Nucl. Instrum. Meth. **A712** (2012) 48, [arXiv:1207.4756](https://arxiv.org/abs/1207.4756).

- [24] Y. Guz *et al.*, *Study of the global performance of an LHCb OT front-end*, CERN-LHCB-2004-120.
- [25] V. Suvorov, G. Van Apeldoorn, I. Gouz, and T. Sluijk, *Avalanche and streamer production in Ar/CO<sub>2</sub> mixtures*, CERN-LHCB-2005-038.
- [26] LHCb collaboration, R. Aaij *et al.*, *Measurement of the track reconstruction efficiency at LHCb*, LHCb-DP-2013-002. to be submitted to Nucl. Instrum. Meth.
- [27] N. Tuning, *Detailed performance of the Outer Tracker at LHCb*, JINST **9** (2014) C01040.
- [28] N. Tuning *et al.*, *Ageing in the LHCb outer tracker: Aromatic hydrocarbons and wire cleaning*, Nucl. Instrum. Meth. **A656** (2011) 45.
- [29] D. van Eijk *et al.*, *Radiation hardness of the LHCb Outer Tracker*, Nucl. Instrum. Meth. **A685** (2012) 62.